SUNGKYU LEE[1*], MIN JUNG KIM[3], NURI CHOI[4], SANG YEON HWANG[2],
SEOK-WOO CHUNG[2], SEUNG-JONG LEE[2], YONGSEUNG YUN[2]

CORROSION BEHAVIOR OF HASTELLOY® C-2000® Ni-Cr-Mo-Fe ALLOYS IN THE ENTRAINED-FLOW COAL GASIFICATION SYNGAS PLANTS

A mechanistic exposure experiment was performed on the commercially available and welded Ni-Cr-Mo-Fe alloy samples used in the piping materials of the coal gasification pilot plant. Thermodynamic Ellingham-Pourbaix stability diagrams were constructed to provide insight into the mechanism of the observed corrosion behavior. The thermodynamic inference on the corrosion mechanism was supplemented with the morphological, compositional and microstructural analyses of the exposed samples using scanning electron microscopy, X-ray diffraction and energy-dispersive X-ray spectroscopy analyses. X-ray diffraction result revealed stable corrosion products of NiO, $MoNi_4$ and $Cr_{4.6}MoNi_{2.1}$ after accumulated total exposure duration of 139 h to the corrosive atmosphere. Scanning electron microscopy and energy-dispersive X-ray spectroscopy positively identified formation of rather continuous and adherent pre-oxidation corrosion products although extensively peeled-off oxides were finally observed as corrosion scales on the post-exposure alloy samples, which were attributed to the chlorination/oxidation into thin (spalled) oxides.

Keywords: Mixed oxidant corrosion; Hastelloy® C-2000® Ni-Cr-Mo-Fe alloy; coal gasification; high temperature halogen corrosion; hydrated chlorides

1. Introduction

Integrated coal gasification combined cycle (IGCC) is a highly efficient and futuristic power generation technology over conventional thermal power generation method for its eco-friendly performance, especially for its feasibility of joint operation with carbon capture and sequestration (CCS) via combined desulfurizer and dust collecting equipment, thus realizing higher CO_2 reduction efficiency [1-2]. Besides, nearly proprietary petroleum-based energy dependence status could be well alleviated via utilization of other fuel sources such as biomass and (industrial) wastes as well as (pulverized) coal resources. Among many such coal gasifiers, the entrained flow gasifier is normally operated at 1200-1550°C and under 2.005 MPa of pressure and 60% CO, 28.4% H_2, 2.5% CO_2, 0.8% CH_4, 600 ppm H_2S, and 110ppm carbonyl sulfide [3]. Such gas composition is also critically affected by the composition of the coal.

An ordinary IGCC plant is comprised of successive units for gasification, syngas purification, combined power generation and oxygen separation. Syngas with major constituents of CO and H_2 is produced in the gasification unit via high temperature and pres-sure reaction of pulverized coal with steam, oxygen in the air and CO_2. More than 99% of the organic constituents of the pulverized coal reactant convert to syngas via reaction with oxygen, steam, and CO_2. Carbon dioxide reacts with carbon to produce carbon monoxide via Boudouard reaction [4]: $C(s) + CO_2(g) = 2 CO(g)$ On the other hand, the ash components mostly form molten slag which flowed down the inner wall of the coal gasifier, rapidly cooled and discharged at the lower part of the gasifier. Pressure vessels and piping materials will be exposed to a broad spectrum of temperature and pressure conditions. Therefore, the composition of process environments and its temperature and dew points have to be quantitatively reviewed and precisely defined. Corrosion and materials selection are thus the key issues in the practical design and operation of the coal gasification plant and the selection of materials of construction and management of corrosion are of prime importance [5]. In the aforementioned coal gasification syngas plant facility affiliated to the Institute for Advanced Engineering (IAE), material wastage and reduction of wall thickness were found extensively on the inner surface of type 316L stainless steel piping [6], which connected the particulate removal unit and water scrubber, which was exposed

[1] DEPARTMENT OF CHEMICAL ENGINEERING, DANKOOK UNIVERSITY, 152 JUKJEON-RO, SUJI-GU, YONGIN-SI, GYEONGGI-DO, 16890, SOUTH KOREA
[2] INSTITUTE FOR ADVANCED ENGINEERING, PLANT ENGINEERING DIVISION, YONGIN-SI, 17180, KOREA (SOUTH)
[3] SUNGKYUNKWAN UNIVERSITY ADVANCED MATERIALS TECHNOLOGY RESEARCH CENTER, SUWON-SI, 16419, KOREA (SOUTH)
[4] HANYANG UNIVERSITY DEPARTMENT OF MATERIALS SCIENCE & CHEMICAL ENGINEERING, ANSAN, 15588, KOREA (SOUTH)

* Corresponding author: sklee@ajou.ac.kr
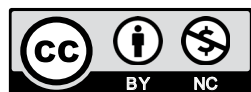
to temperature range of 150 to 180℃. More specifically, a representative halogen corrosion mechanism was experimentally substantiated [6-8] to explain the observed material wastage and corrosion behavior, i.e., formation of discontinuous (complex) oxide phases and subsequent chlorine-induced active oxidation under the predominantly reducing environment encountered in the coal gasification syngas plant as previously specified [6-8].

Therefore, the piping in that location is especially susceptible to mixed oxidant corrosion at temperature of 150 to 180℃ and the C-2000 Ni-Cr-Mo-Fe alloy samples were obtained from Haynes® International for their extremely high resistance to hydrochloric and sulfuric acids as well as pitting and crevice corrosion.

2. Experimental

Upon completion of the corrosion exposure test for a specified duration of time, the samples were retrieved from the coal gasification syngas plant piping to obtain their (surface) morphological, compositional, and cross-sectional information via SEM/EDS and low angle X-ray diffraction analyses for subsequent discussion. Composition of the sub-bituminous coal samples is listed in Table 1 as a basis for possible sources of foreign impuri-

TABLE 1

Physical properties of the sub-bituminous coal samples used in the present study: V.M., F.C., IDT, ST, HT, FT mean volatile matter, fixed carbon, initial deformation temperature, softening temperature, hemispherical temperature, and fluid temperature, respectively. KPU and WH mean names of commercially available coal feed-stocks, generically nominated after their location of coal mines. The full names of the KPU and WH could not be further inquired, considering limited supply from a proprietary source

Physical Properties	Coal samples	KPU	WH
Proximate analysis (dry–basis, wt%)	V. M.	55.62	32.13
	F. C.	38.58	48.67
	Ash	5.8	19.2
Ultimate analysis (ash–free wt%)	C	76.11	87.99
	H	5.28	5.7
	O	16.79	3.05
	N	1.27	1.94
	S	0.49	1.32
Heating value (HHV)	kcal/kg	6,570	6,628
Inorganic composition analysis (wt%)	SiO_2	36.63	55.44
	Al_2O_3	20.79	31.39
	Fe_2O_3	7.99	4.44
	CaO	19.42	5.24
	MgO	6.06	0.71
	Na_2O	6.58	0.29
	K_2O	1.57	0.71
	TiO_2	0.78	1.53
Ash fusion temperature (℃)	IDT	1,168	1,290
	ST	—	—
	HT	1,208	1,394
	FT	1,220	1,412

ties observed in the SEM/EDS analyses results of the subsequent section on "characterizations". These characterization analyses were methodically, intensively and repeatedly performed to characterize the observed corrosion products and to provide insight into the mechanism of the observed corrosion behavior occurring in the exposed location of the coal gasification plant.

Sample preparation

The C-2000 Ni-Cr-Mo-Fe alloy samples were obtained from Haynes® International in planar rectangular geometry. Nominal composition of test alloy was provided by the manufacturer and no additional compositional analysis was made. Composition of the tested C-2000 Ni-Cr-Mo-Fe alloy is listed in Table 2. The test samples were cut into desired sizes of 76 mm (length) × 36 mm (width) × 3 mm (thickness) for subsequent pre-oxidation treatment at 400℃ under stagnant air atmosphere for 24 h. Pre-oxidation was performed using a tube furnace where sample was located inside middle of an alumina tube. The sample was N_2-purged for 10 h at room temperature. The alumina tube was subsequently exposed to ambient air by detaching air tight nitrogen purge mechanism before being heated to 400℃. After 24 h of pre-oxidation at 400℃ in air, the sample was air-cooled to room temperature in the furnace. The edge of the pre-oxidized samples with 36 mm width was properly welded against the inside of the 316L stainless steel piping at the back-end portion of the filter system in the coal gasification syngas plant located at Taean, west coast of South Korea, the internal part of which was exposed to 170℃, as schematically specified in the previously published journal articles [6-8]. The welding of the corrosion test sample against the 316L stainless steel inner piping was performed so that the syngas stream was parallel to the 76 mm × 36 mm surface of the sample as specified in the previous publications [7,8].

TABLE 2

Nominal composition of Haynes® Hastelloy® C-2000® Ni-Cr-Mo-Fe alloy

Constituent	Wt.%
Ni	59
Cr	23
Mo	16
Fe	3
Cu	1.6
Al	0.5
Mn	0.5
Si	0.08
C	0.01

The corrosion test sample was thus intermittently exposed to 170℃, 2 MPa of coal syngas composition in Table 3 for total accumulated duration of 139 h. The pre-oxidized and post-exposure samples were fitted into plastic mounting tubes of 35 mm OD and 10 mm height to hold epoxy resin prepared at 1:1 proportion of SpeciFix® resin and SpeciFix®-40 curing agent. Three post-

exposure samples were consecutively cold-mounted, ground, and polished on a variable speed rotating wheel grinder-polisher. Grinding was thus performed with rotating SiC papers from #200 to 2000, and the mounted samples were subsequently polished with a rotating cloth soaked with a suspension of alumina (Al_2O_3) particles (size: 0.3 and 1 μm).

Etching solution was prepared from reagent grade acids to approximate composition of aqua regia, i.e., 20 mL HNO_3 and 60 mL HCl for 80 mL total volume. The sample was etched for 30 sec ~ 1 min, depending on the state of etched surface as observed by optical microscope. Etching was repeated maximum 3 times as necessary.

TABLE 3

Input gas composition ranges corresponding
to the coal syngas production plant

CO	42-45%
H_2	22-25%
CO_2	4-6%
N_2	10-20%
H_2S	1000ppm
Particulate materials	10,000 mg/m^3
HCl	7 ppm
H_2O	5 %
CH_4	2-3 %
COS	100 ppm

3. Results and discussion

Thermodynamic perspectives

To comprehensively define actual corrosion environment encountered in the present study, dew point of the process gas stream as specified in Table 3 was repeatedly ascertained using the commercial thermochemical software and the result was 78.6°C, which is lower than the reaction temperature of 170°C encountered by the C-2000 alloy. In view of this, possibility of dew point corrosion is rather reasonably excluded from the possible cause of the observed corrosion behavior for the C-2000 alloy of the coal gasification plant facility. Similar conclusion was also drawn in the previous publication [6]. As a starting point, a general Ellingham-Pourbaix type phase stability diagrams were prepared using the FactSage® software ver. 7.0 to investigate into the thermodynamic stability of metal chlorides and oxides at the test temperature for quantitative definition of the corrosion environments and thermodynamically stable metal oxides and chlorides prevailing under these mixed oxidant corrosion environments of the coal gasification syngas plant. Thermodynamically stable reaction products expected from the corrosion exposure tests performed on the C-2000 Ni-Cr-Mo-Fe alloy samples are listed in Table 4.

Fig. 1 illustrates areas of thermodynamically stable reaction products from the mixed oxidant corrosion of the C-2000 Ni-Cr-Mo-Fe alloy samples at 170°C for exposure samples re-

TABLE 4

The phases of reaction 26 are stable for the corrosive environment depicted by the gray solid dot in the Fig. 1 as indicated by the large and bold arrow–mark which represents the partial pressures of chlorine and oxygen calculated using the actual corrosive environments of mixed oxidants encountered in the present research. The sub-table shows numerical values of partial pressures of chlorine and oxygen. Detailed reaction products corresponding to the areas given by numbers in the phase stability diagram in the Fig. 1 are listed below. The "S2" in "MCl$_2$_S2" and "FCC_S2" means a secondary solid form

pO$_2$	pCl$_2$
6.1584 ×10^{-49} atm	5.3523 × 10^{-30} atm

|	
1)	$MCl_2 + Al_2SiO_5 + CuCl + Al_2O_3 + MoO_2 + MCl_2\_S2 + Cr_2O_3$
2)	$MCl_2 + Al_2SiO_5 + CuCl + Cr_2O_3 + Al_2O_3 + MoO_2 + MCl_2\_S2 + Fe_2O_3$
3)	$MCl_2 + Al_2SiO_5 + CuCl + Cr_2O_3 + Al_2O_3 + MnO(MoO_3) + MoO_2 + Fe_2O_3$
4)	$MCl_2 + Ni_2SiO_4 + CuCl + Cr_2O_3 + Al_2O_3 + MnO(MoO_3) + MoO_2 + Fe_2O_3$
5)	$MoO_2 + CuCl + NiO + Fe_2O_3 + Cr_2O_3 + Al_2O_3 + MnO(MoO_3) + Cr_2O_3 + Ni_2SiO_4$
6)	$MCl_2 + CuCl + Fe_2O_3 + Cr_2O_3 + Al_2O_3 + MoO_2 + MCl_2\_S2 + Ni_2SiO_4$
7)	$MCl_2 + CuCl + NiO + Fe_2O_3 + Cr_2O_3 + Al_2O_3 + MoO_2 + Ni_2SiO_4$
8)	$NiO + Cr_2O_3 + MoO_2 + Fe_2O_3 + CuCl + MnO(MoO_3) + Al_2O_3 + Mn_3Al_2Si_3O_{12}$
9)	$NiO + Cr_2O_3 + MoO_2 + Cu_2O(Fe_2O_3) + Fe_2O_3 + MnO(MoO_3) + Al_2O_3 + Ni_2SiO_4$
10)	$NiO + Cr_2O_3 + MoO_2 + Cu_2O(Fe_2O_3) + Fe_2O_3 + MnO(MoO_3) + Al_2O_3 + Mn_3Al_2Si_3O_{12}$
11)	$MoO_2 + Mn_3Al_2Si_3O_{12} + MnAl_2O_4 + CuCl + Fe_2O_3 + Cr_2O_3 + Al_2O_3 + NiO$
12)	$NiO + Cr_2O_3 + MoO_2 + Cu_2O(Fe_2O_3) + Fe_2O_3 + MnAl_2O_4 + Mn_3Al_2Si_3O_{12} + Al_2O_3$
13)	$MCl_2 + Mn_3Al_2Si_3O_{12} + CuCl + Fe_2O_3 + Cr_2O_3 + Al_2O_3 + MoO_2 + NiO$
14)	$MCl_2 + Mn_3Al_2Si_3O_{12} + Fe_2O_3 + Cr_2O_3 + Al_2O_3 + MoO_2 + FCC + NiO$
15)	$MCl_2 + Fe_2O_3 + Cr_2O_3 + Al_2O_3 + MoO_2 + FCC + MCl_2\_S2 + Ni_2SiO_4$
16)	$MCl_2 + Al_2SiO_5 + Cr_2O_3 + Al_2O_3 + MoO_2 + FCC + MCl_2\_S2 + Fe_2O_3$
17)	$MCl_2 + Al_2SiO_5 + Al_2O_3 + MoO_2 + FCC + MCl_2\_S2 + Cr_2O_3$
18)	$MCl_2 + NiO + Fe_2O_3 + Cr_2O_3 + Al_2O_3 + MoO_2 + FCC + Ni_2SiO_4$
19)	$MCl_2 + Al_2SiO_5 + Al_2O_3 + MoO_2 + FCC + FCC\_S2 + Cr_2O_3$
20)	$MCl_2 + Cr_2O_3 + Cr_2O_3 + Al_2O_3 + MoO_2 + FCC + FCC\_S2 + Fe_3Al_2Si_3O_{12}$
21)	$MCl_2 + Cr_2O_3 + Al_2O_3 + MoO_2 + FCC + FCC\_S2 + Fe_2SiO_4$
22)	$MCl_2 + Fe_2O_3 + Cr_2O_3 + Al_2O_3 + MoO_2 + FCC + MCl_2\_S2 + Fe_2SiO_4$
23)	$MCl_2 + Fe_2O_3 + Cr_2O_3 + Al_2O_3 + MoO_2 + FCC + FCC\_S2 + Fe_3Al_2Si_3O_{12}$
24)	$MCl_2 + Al_2SiO_5 + Cr_2O_3 + Al_2O_3 + MoO_2 + FCC + FCC\_S2 + Fe_2O_3$
25)	$MCl_2 + Fe_2O_3 + Cr_2O_3 + Al_2O_3 + MoO_2 + FCC + FCC\_S2 + Ni_2SiO_4$
26)	$MCl_2 + Mn_3Al_2Si_3O_{12} + Cr_2O_3 + Al_2O_3 + MoO_2 + FCC + FCC\_S2 + Fe_2O_3$
27)	$FCC + Mn_3Al_2Si_3O_{12} + MnAl_2O_4 + Cr_2O_3 + Al_2O_3 + MoO_2 + FCC\_S2 + Fe_2O_3$
28)	$FCC + Mn_3Al_2Si_3O_{12} + MnAl_2O_4 + Fe_2O_3 + Cr_2O_3 + Al_2O_3 + MoO_2 + NiO$
29)	$gas + Mo_4O_{11} + NiO + Fe_2O_3 + Cr_2O_3 + Al_2O_3$
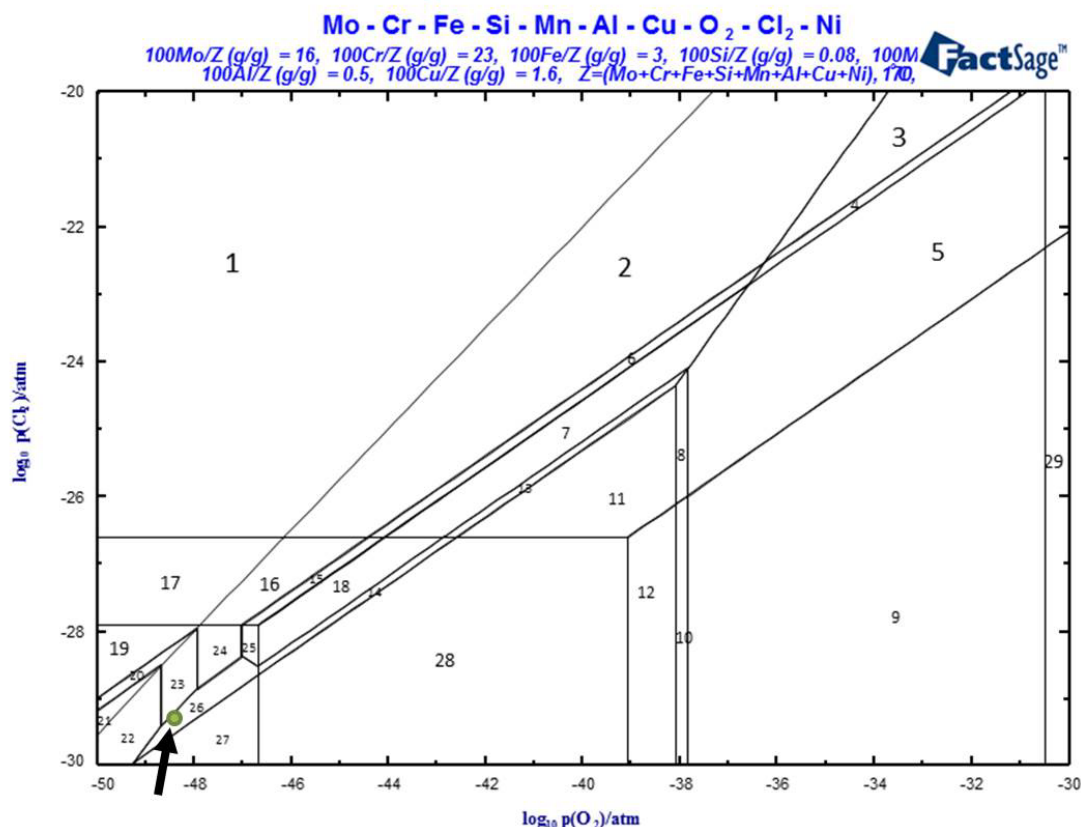
Fig. 1. Stability diagram calculated using a commercially available thermochemical software at 170℃, with ordinate and abscissa representing the partial pressures of chlorine and oxygen, respectively. Detailed reaction products corresponding to the areas given by numbers in the phase stability diagram are listed in Table 4

covered from the coal gasification plant. The calculated partial pressures of chlorine and oxygen, as marked by the gray dot in Fig. 1 and supplemented as a sub-table in Table 4, represent predominantly reducing environment of the coal gasification syngas process stream. Table 4 also lists the thermodynamically expected reaction products corresponding to the numbered areas in Fig. 1. Thermodynamic feasibility of metal sulfides formation was also considered and subject to rigor of repeated FactSage® modeling but metal chlorides were the only reaction products expected therefrom. The possibility of metal sulfides formation was thus further investigated via subsequent surface elemental SEM/EDS analyses. Standard Gibbs free energy data were also comprehensibly quoted [9] for manual cross-checking and metal chlorides formation was finally corroborated as predominating. In view of these, thermodynamic credibility of the phase stability diagram in Fig. 1 is rather cogently substantiated although possibility of metal sulfides formation necessitates further experimental substantiation.

Characterization of the pre-oxidized samples

Since the pre-oxidation procedure was performed under pure stagnant air atmosphere as described in the previous section on sample preparation, the pre-oxidation products were expected to predominantly consist of oxides and complex oxides [10]. The presence of NiO was expected by the thermodynamic Ellingham-Pourbaix stability diagrams in Fig. 1 and corresponding stable reaction products formed during the pre-oxidation procedure at higher oxygen partial pressure as summarized in Table 4. Fig. 2 shows SEM micrograph of pre-oxidized C-2000 alloy. EDS average surface elemental composition over the area presented in Fig. 2 is listed in Appendix 1 which is quite representative of the bulk composition of the C-2000 alloy. Therefore, suitable agreement between the bulk and surface composition as experimentally substantiated in the Fig. 2 and Appendix 1 gave partial justification of the present FactSage® modeling approach although surface effects on the FactSage® modeling warrant further research. The scratch marks from the SiC papers are clearly visible in Fig. 2 and the EDS analysis result in Appendix 1 revealed an approximate surface compositional result of 57Ni-16Mo-21Cr-5O (wt%). The comparatively lower average surface oxygen composition as shown in Appendix 1 implies very slight degree of oxidation, mostly via formation of uniformly thin and adherent complex surface oxides of approximately 40-75 nm observed for the 304 stainless steel, closely following the arguments of Spiegel et al. [10]. The absence of Fe in Appendix 1 is attributed to experimental uncertainty although EDS average chemical composition analyses over the area of post-exposure samples presented in Fig. 3 do identify

Fe as supplemented in Appendix 2. Equilibrium vapor pressures of MoO, MoO$_3$, and MoO$_2$ were calculated using commercially available FactSage FactPC, FToxid, and FSstel thermochemical databases for possible formation and evaporation of molybdenum oxides [10]. The calculated equilibrium vapor pressures of the molybdenum oxides at 400°C are negligibly small, as low as 3.9×10^{-21}, 4.5×10^{-42}, and 6.05×10^{-63} atm for MoO$_3$, MoO$_2$ and MoO, respectively.
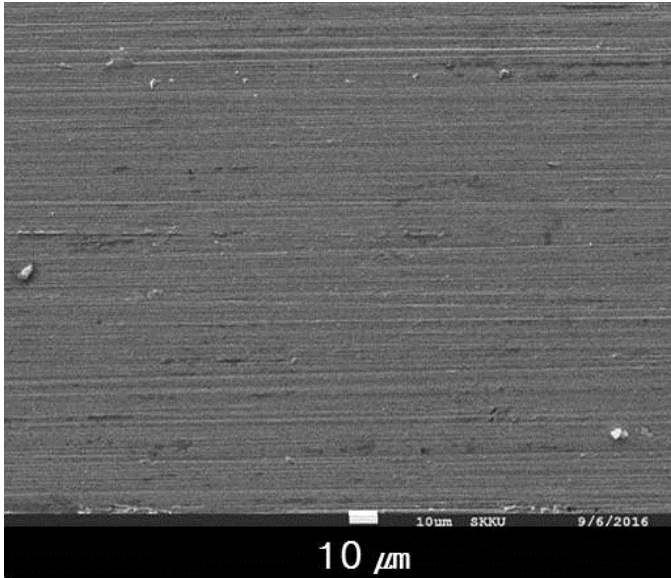

Fig. 2. SEM/EDS micrograph of a pre-oxidized C-2000 Ni-Cr-Mo-Fe alloy sample

Chromium contents of 23 wt% in the C-2000 alloy is significantly higher than the critical chromium level of 7 wt% required for the formation of a uniformly spread layer over the entire surface, which was also observed for the Haynes® Hastelloy® C-4 alloy [11].

Pre-oxidation treatment at 400°C and 24 h exposure under stagnant air was based on the literature data by Spiegel et al. [10] on the 304 stainless steel and pure Fe, Cr, Ni samples, where 40-75 nm of complex (Cr, Fe)$_2$O$_3$ oxide was observed to form on the 304 stainless steel by X-ray photo-electron spectroscopy (XPS). Pre-oxidation treatment is usually performed at the same

or lower temperatures of actual exposure tests [10,11,13]. Although pre-oxidation process performed in the present research could be regarded as redundant, reproducible pre-treatment of the sample surface was originally intended. However, actual pre-oxidation data for C-2000 alloy at this exposure condition were not available and the approximate thickness of oxide and its composition were thus qualitatively inferred by comparison with literature [10]. In view of the overall composition of C-2000 alloy, predominantly Cr$_2$O$_3$ was anticipated with very little proportion of Fe$_2$O$_3$. Judging from the oxygen affinity of the constituent elements, the pre-oxidation process probably formed outer Ni-rich (Cr$_2$O$_3$-MoO$_2$-NiO) and Cr-rich (Cr$_2$O$_3$-MoO$_2$-NiO) in the inner part, considering the lowest equilibrium partial pressure of oxygen for Cr$_2$O$_3$ [4,9]. It is now evident that quantitative interpretation of the pre-oxidation treatment and its consequence warrants further methodical and mechanistic experimental research although protective nature of the pre-oxidized surface scales was subsequently examined and analyzed using the post-exposure samples via SEM/EDS analysis in the following section on "characterization of the post-exposure samples".

Examination and characterization of the post-exposure C-2000 Ni-Cr-Mo-Fe alloy samples by SEM/EDS and X-ray diffraction (XRD)

Fig. 3a shows that large corrosion product scales with sizes in the tens of micro-meter range were found in randomly grown flake forms, predominantly revealing peeled-off and spalled morphology. On the other hand, Fig. 3b and Fig. 3c show that the surface corrosion products did not consist of a homogeneous films in nano-meter range as discussed in the literature [10]. Presence of the internal Cr-rich (Cr$_2$O$_3$-MoO$_2$-NiO) oxide is partially substantiated from the individual element-wise EDS peaks as captioned in the Appendix 2b and Appendix 2c. On the other hand, Appendix 2 also reveals slightly different surface atomic proportion of alloying elements from that of the pre-exposure sample (see Appendix 1). Although individual identities of the surface corrosion products are not easily distinguishable from the Fig. 3a-c, they are strongly inferred from the thermodynamically expected corrosion reaction products listed in number 26

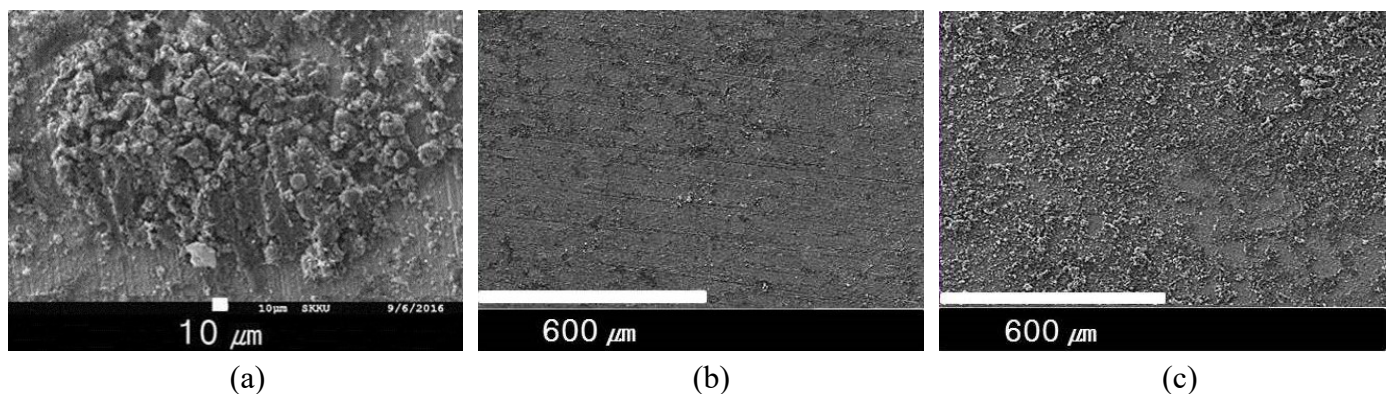| (a)	(b)	(c)

Fig. 3. SEM/EDS micrographs of post-exposure alloy samples

in Table 4, i.e., mostly metal chloride, oxides and spinel. Typical SEM micrograph of C-2000 Ni-Cr-Mo-Fe alloy sample is shown in Fig. 4, revealing its grain boundaries treated with a suitable etchant and under most favorable etching condition and a representative low angle X-ray diffraction result of Fig. 5 conspicuously shows NiO, $MoNi_4$ and $Cr_{4.6}MoNi_{2.1}$ peaks of the surface corrosion products. Although NiO peak was previously explained in "characterization of the pre-oxidized sample", the formation of intermetallic compounds $MoNi_4$ and $Cr_{4.6}MoNi_{2.1}$ could not be explained by SEM micrographs in Fig. 3 and corresponding average surface compositional EDS results of Appendix 2. In Fig. 3 and Appendix 2, the atomic and weight percent of Mo could not be unequivocally distinguished in the latter. More specifically, Appendix 2a shows EDS analysis of average chemical composition over the magnified area in Fig. 3a. However, a point analysis or elemental EDS mapping was not performed for Appendix 2a, b, and c due to experimental constraints. Additionally, EDS analysis results in Appendix 2 should be interpreted with caution and reservation with due consideration of effect
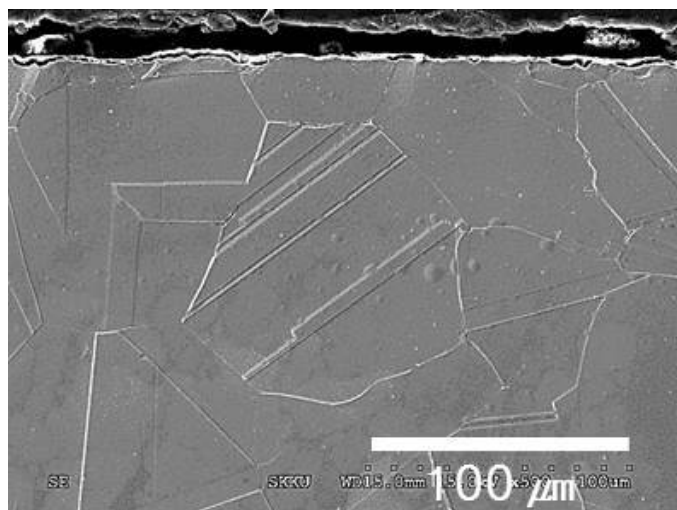
of signal interference from the alloy substrate core, which also warrants further research. The origin of sulfur in Appendix 2a is most probably attributed to particulates of the sub-bituminous pulverized coal samples which were mechanically carried over in the syngas process stream.

Effect of increased chromium contents decreases oxidation by selective oxidation of chromium and formation of a protective scale containing Cr_2O_3 [12], which is attributed to high oxygen affinity of chromium and this is experimentally substantiated by Fig. 6a. As for surface and cross-sectional EDS analysis results of Mo, its bulk and surface contents in atomic % remained almost the same prior to (8.89) and post (7.26) exposure as shown in Appendix 1 and Table 5, respectively. However, possibility of overlapping EDS peaks of elemental sulfur and molybdenum also exists as represented in Fig. 6b and c, which warrants further research.

Fig. 4. Typical microstructure of Haynes® Hastelloy® C-2000® Ni-Cr-Mo-Fe alloy sample

TABLE 5

Weight and atomic percent of individual EDS analyses results of Fig. 6i is analyzed and tabulated

Element	Weight %	Atomic %
O	8.35	25.10
Al	2.27	4.04
S	0	0
Cl	0	0
Cr	21.52	19.90
Ni	53.37	43.70
Mo	14.5	7.26
Total	100	100

In view of Fig. 6, it was quite evident that the possibly overlapped sulfur and molybdenum peaks should be more convincingly explained for quantitative insight into the identity of the surface corrosion product scales. Table 5 thus shows (cross-sectional) surface elemental Ni and Mo atomic ratios of 43.7/7.26, approximately accounting for the stoichiometric elemental ratio of $MoNi_4$. In view of only one NiO peak in Fig. 5, identification of NiO is only partially substantiated in conjunction with thermodynamically expected reaction products in Table 4 using FactSage® software ver. 7.0. However, NiO was most probably formed during pre-oxidation procedure and retained during subsequent exposure test as discussed in the previous section on "pre-oxidation", which is also partially justified by elemental presence of Ni in Fig. 6d. Surface elemental EDS mapping result in the Appendix 2a revealed that Al, Si, and Ca were detected as well as Fe and Ni. In view of the inherent composition of the C-2000 Ni-Cr-Mo-Fe alloy samples, the origin of Ca, Al, and Si is again attributed to particulates of the sub-bituminous pulverized coal samples mechanically carried over in the syngas process stream as listed in Table 1: SiO_2, CaO, and Al_2O_3 are thus explained as main ingredients of the solid oxide particulates in rather noticeable quantities, contributing to the observed EDS result in Appendix 2a. Considering original composition of the C-2000 Ni-Cr-Mo-Fe alloy samples, presence of Si in significant surface composition of 7.48 atomic%
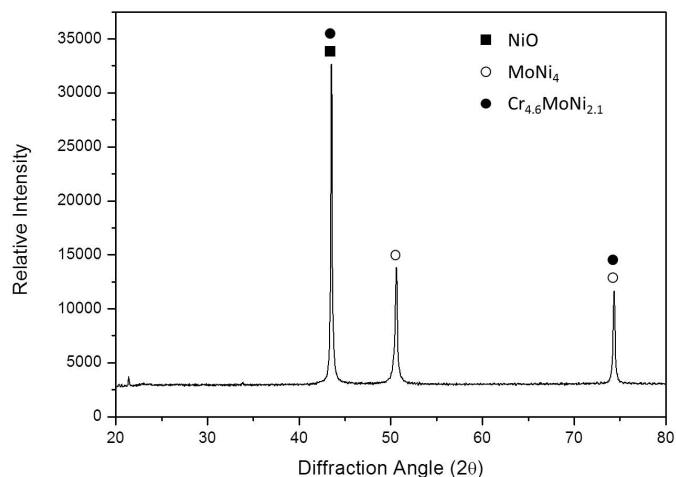

Fig. 5. Low angle X-ray diffraction result of the post-exposure Haynes® Hastelloy® C-2000® Ni-Cr-Mo-Fe alloy sample
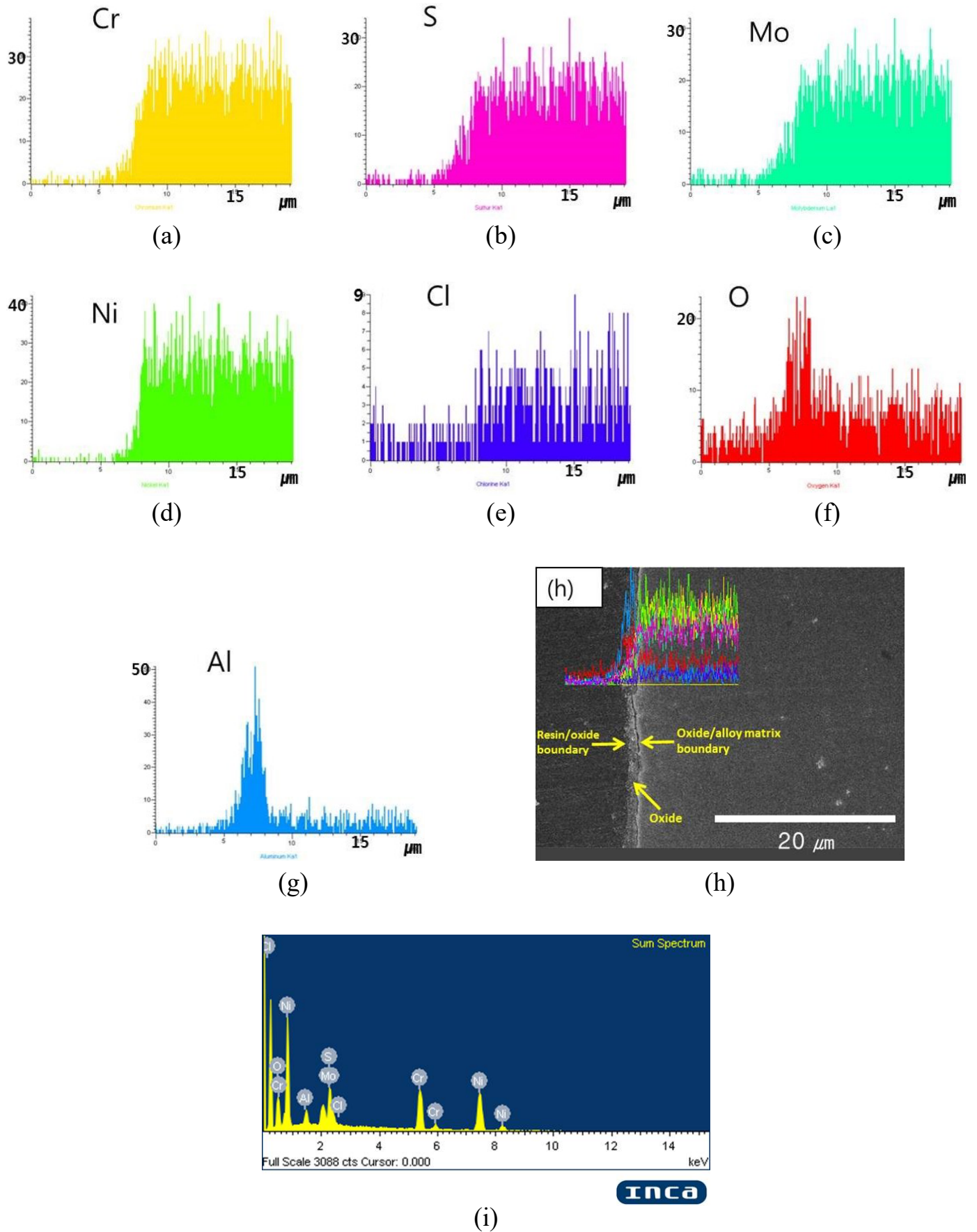
Fig. 6. (a)-(g) represent EDS peaks of respective elements as captioned. The ordinate and abscissa represent peak intensity in count(s) per second (CPS) and thickness in μm. (h) Higher magnification SEM-EDS analysis result of cross-sectional microstructure of an exposed C-2000 sample: The boundary lines indicated by the bold yellow arrow-marks represent demarcation between the epoxy resin to the left and the cross-section of the post-exposure sample to the right. The oxide scale is separately indicated by the third arrow mark. (i) is corresponding EDS spectra

(tabulated result in the Appendix 2a) excludes possibility of its origin from the bulk alloy because inherent Mn composition in the alloy sample was higher than Si but Mn was not detected in Appendix 2a. Similar reasoning also excludes possible contribution of bulk Al alloying element to the tabulated EDS result in Appendix 2a. However, detection of Cr in the tabulated EDS results in Appendix 2b and Appendix 2c confirm its origin from the bulk alloy because Cr does not exist in the coal samples as represented in Table 1. The higher magnification SEM/EDS micrograph in Fig. 3a should thus be accounted for in more comprehensive way.

Further SEM/EDS analyses were comprehensively and intensively performed to experimentally substantiate the presence of the metal chlorides at the oxide/metal interface and the result shown in Fig. 6e. Among possible metallic elements of Ni, Mo, Cr, Fe, Al, Mn, Si to fit into M in MCl_2 (s), chlorides of Cr (melting point (m.p.) = 815°C), Al (m.p. = 192.4°C), Mo (m.p. = 194°C) and Fe (m.p. = 306°C) are strongly inferred from thermodynamic calculations of Table 4 via FactSage® software ver. 7.0. Although melting points are higher than or similar to the process stream temperature of 170°C employed in the present study, the temperature at which the vapor pressure of Al chloride is approximately equal to 10^{-4} atm are almost equivalent to or significantly lower than process temperature of 170°C except for high-melting chromium chloride [9]. Therefore, the observed corrosion phenomena are explained as follows: In the predominantly reducing environment of the present research, oxide phases could be absent or discontinuous and metal chlorides could form directly on the metal surface or more favorably at the oxide/metal interface where partial pressure of oxygen could become very low. The metal chloride is subsequently transformed into oxides, which is strongly inferred from the suggested reaction 24 in Table 4. Al_2O_3 formation is highly suspected in view of Fig. 6e, f and g and this is attributed to transformation of aluminum chloride into oxide, following the previous arguments. In view of this, the observed SEM micrographs in Fig. 3, EDS analyses results in Appendix 2 and Fig. 6 are explained in terms of metal chloride formation at the oxide/metal interface where partial pressure of oxygen could be quite low. The metal chloride MCl_2 is thermodynamically expected from Table 4 under the reducing atmosphere of the present study, which is also marked by the gray dot in the Fig. 1.

The observed corrosion products in Fig. 3a are thus partially justified by evaporation of the low-melting metal chlorides and subsequent spallation and peeling-off of the corrosion scales. Vaporized aluminum chloride is most probably accounted for as illustrated in Fig. 6e, Fig. 6f and Fig. 6g.

Electron beam energy during the EDS analysis was not made known at the time but oxide scale thickness is to be inferred from Fig. 6h where boundaries of resin/oxide and oxide/alloy matrix are clearly demarcated. Due to experimental constraints, EDS mapping results could not be retrieved either and EDS spectra in Fig. 6i were not supplemented. However, similar presentation of EDS spectra was made in the previous publication and corrosion mechanism was inferred with reasonable certainty

[6]. As an additional corroboration of suggested chlorination/oxidation into thin (spalled) oxides, melting points of the ternary CaO-SiO_2-Al_2O_3 system was calculated using the available database of the FactSage® software ver. 7.0. The phase diagram of ternary Al_2O_3-SiO_2-CaO system is graphically constructed in Fig. 7, where T(min) = 1184.3°C is marked in the upper left portion with corresponding composition of 61.5wt%SiO_2-25.1wt%CaO-13.4wt%Al_2O_3. Therefore, the observed SEM/EDS micrographs of Fig. 3 and Fig. 6 are explained in terms of metal chloride formation at the oxide/metal interface, where the partial pressure of oxygen could be quite low [14,15].

Lastly, possibility of sulfide formation was strongly suspected in view of the input gas composition as listed in Table 3 but it was not experimentally substantiated by the low angle X-ray diffraction data in Fig. 5 although some trace of elemental sulfur was detected in Fig. 6b.

4. Summary and engineering significance

A corrosion exposure study was performed for the commercially available C-2000 Ni-Cr-Mo-Fe alloy samples under coal-gasifying plant facilities located at Taean, southwest coast of South Korea. The morphological and microstructural analyses were made on the exposed corrosion samples using SEM/EDS examinations and thermodynamic calculations based on the FactSage® software ver. 7.0. The observed material wastage was attributed to the combined effects of evaporation of hydrated metal chlorides of Fe, Al, and Cr and subsequent transformation into thin (spalled) oxides.

REFERENCES

[1] A.F. Ghoniem, Prog. Energ. Combus. **37**, 15-51 (2011).
[2] J. Hetland, R. Anantharaman, Energy Sustain. Dev. **13**, 56-63 (2009).
[3] J. Huang, I. Dincer, Int. J. Hydrogen Energ. **39**, 3294-3303 (2014).
[4] N. Birks, G.H. Meier, Introduction to High Temperature Oxidation of Metals, 1983 Edward Arnold, London.
[5] A. Zahs, M. Spiegel, H.J. Grabke, Corros. Sci. **42**, 1093-1122 (2000).
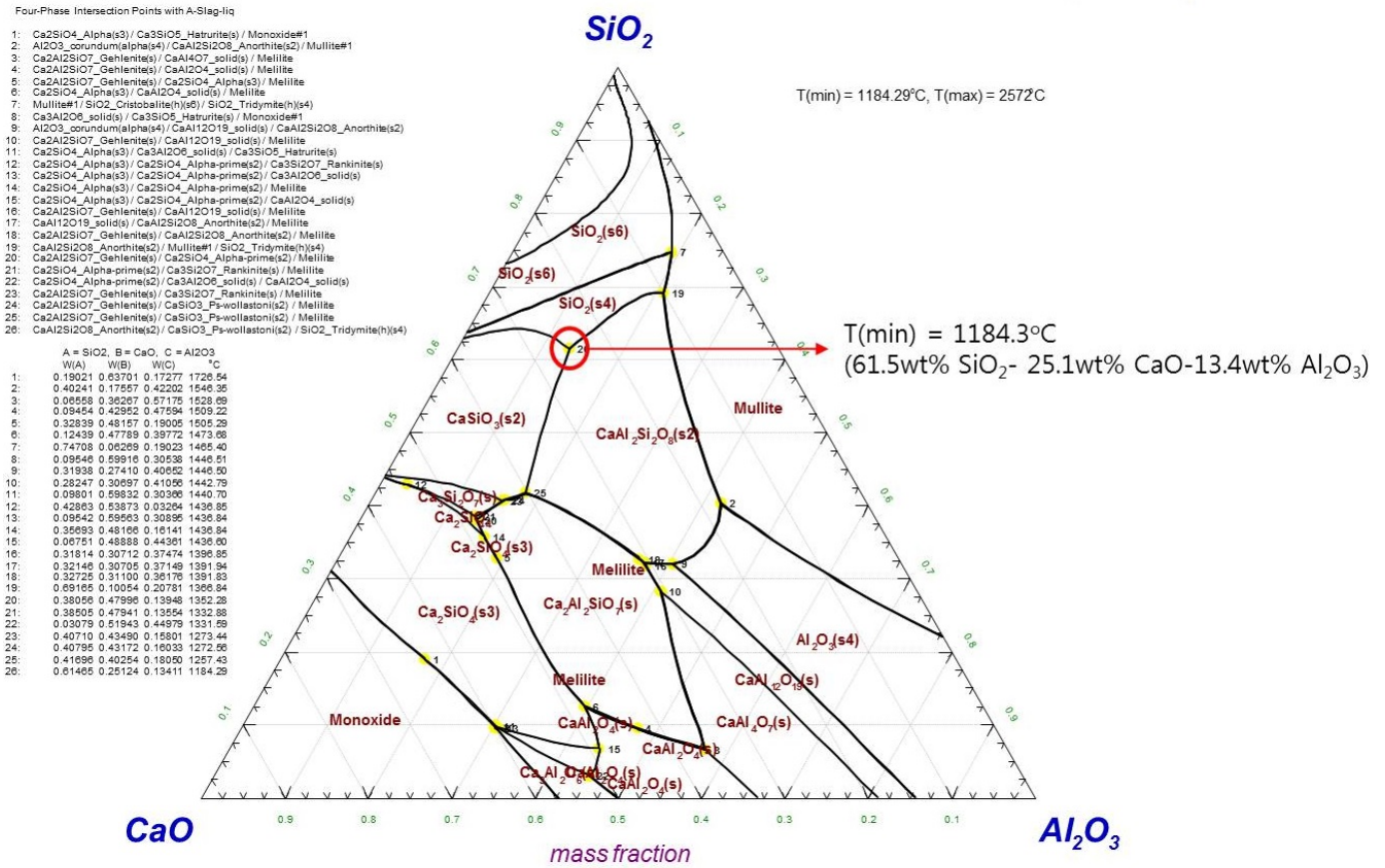
Fig. 7. Ternary phase diagram of the CaO-SiO$_2$-Al$_2$O$_3$ system was graphically constructed via the FactSage® software ver. 7.0

[6] S. Lee, S.-W. Chung, S.-J. Lee, Y. Yun, Corrosion **69**, 921-935 (2013).

[7] S. Lee, M. J. Kim, J. Lee, S.-H. Kang, S.-J. Lee, Y. Yun, Materials Testing **57**, 409-416 (2015).

[8] S. Lee, M.J. Kim, J. Lee, S.-H. Kang, S.-J. Lee, Y. Yun, Materials Testing **57**, 543-550 (2015).

[9] E.T. Turkdogan, Physical Chemistry of High Temperature Technology, 1980 Academic Press, New York.

[10] H. Asteman, M. Spiegel, Corros. Sci. **49**, 3626-3637 (2007).

[11] N. Hussain, K.A. Shahid, I.H. Khan, S. Rahman, Oxid. Met. **41**, 251-269 (1994).

[12] V.B. Trindade, R. Borin, B.Z. Hanjari, S. Yang, U. Krupp, H.-J. Christ, Mat. Res. **8**, 365-369 (2005).

[13] B. Önay, Y. Saito, Oxid. Met. **40**, 65-83 (1993).

[14] P.L. Daniel, R.A. Rapp, Advances in Corrosion Science and Technology, M.G. Fontana, R.W. Staehle (Eds.): Halogen Corrosion of Metals, Vol. 5, Plenum Press, New York, USA (1976), pp. 55-172.

[15] S. Lee, K. Maemura, T. Yamamura, S. Nakazawa, K.H. Lee, D. Chang, J.-H. Ahn, H. Chung, Corrosion **62**, 13-28 (2006).

Appendices

Element	Weight%	Atomic%
O	5.24	17.40
Cr	21.54	22.01
Ni	57.16	51.70
Mo	16.05	8.89
Totals	100.00	

Appendix 1. Average chemical composition by EDS over the area presented in Fig. 2

Element	Weight%	Atomic%
O	37.10	55.91
Al	2.77	2.48
Si	8.72	7.48
S / Mo	36.47	27.43
Ca	2.07	1.25
Fe	7.74	3.34
Ni	5.13	2.11
Totals	100.00	

(a)

Element	Weight%	Atomic%
O	12.18	34.74
Al	0.47	0.79
Si	0.49	0.80
Cr	20.37	17.87
Fe	1.32	1.07
Ni	45.57	35.40
Mo	19.60	9.32
Totals	100.00	

(b)

Element	Weight%	Atomic%
O	23.76	50.11
Al	1.10	1.38
Si	1.98	2.37
Cr	20.13	14.11
Fe	5.06	3.06
Ni	30.82	17.72
Mo	17.15	11.25
Totals	100.00	

(c)

Appendix 2. a, b, and c represent average chemical composition by EDS analyses over the area presented in Fig. 3a, b, and c, respectively